IOPscience iopscience.iop.org

Home Search Collections Journals About Contact us My IOPscience

Cross-sectional scanning thermal microscopy of ErAs/GaAs superlattices grown by molecular beam epitaxy

This content has been downloaded from IOPscience. Please scroll down to see the full text.

2015 Nanotechnology 26 265701

(http://iopscience.iop.org/0957-4484/26/26/265701)

View the table of contents for this issue, or go to the journal homepage for more

Download details:

IP Address: 128.62.36.214

This content was downloaded on 06/07/2015 at 21:17

Please note that terms and conditions apply.

**IOP** Publishing Nanotechnology

Nanotechnology **26** (2015) 265701 (5pp) doi:10.1088/0957-4484/26/26/265701

# Cross-sectional scanning thermal microscopy of ErAs/GaAs superlattices grown by molecular beam epitaxy

**K W Park, E M Krivoy, H P Nair, S R Bank and E T Yu**

[1] Microelectronics Research Center, University of Texas at Austin, 10100 Burnet Rd., Austin, TX 78758, USA

E-mail: ety@ece.utexas.edu

Received 26 February 2015, revised 27 April 2015
Accepted for publication 14 May 2015
Published 9 June 2015

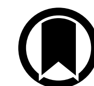


**Abstract**

Scanning thermal microscopy has been implemented in a cross-sectional geometry, and its application for quantitative, nanoscale analysis of thermal conductivity is demonstrated in studies of an ErAs/GaAs nanocomposite superlattice. Spurious measurement effects, attributable to local thermal transport through air, were observed near large step edges, but could be eliminated by thermocompression bonding to an additional structure. Using this approach, bonding of an ErAs/GaAs superlattice grown on GaAs to a silicon-on-insulator wafer enabled thermal signals to be obtained simultaneously from Si, $SiO_2$, GaAs, and ErAs/GaAs superlattice. When combined with numerical modeling, the thermal conductivity of the ErAs/GaAs superlattice measured using this approach was $11 \pm 4$ W $m^{-1}$ $K^{-1}$.

Keywords: scanning thermal microscopy, ErAs/GaAs superlattice, thermal conductivity

(Some figures may appear in colour only in the online journal)

## 1. Introduction

Developments in the understanding and engineering of thermal properties of materials at the nanoscale [1–9] have led to increased interest in methods for quantitative characterization of thermal transport behavior with high spatial resolution [10–12]. Among the different types of nanostructures exhibiting altered thermal transport behavior compared to their bulk-like counterparts, crystalline semiconductors in which nanoparticles or other nanoscale structures are incorporated via epitaxial growth are of particular interest due to their potential for use in thermoelectric devices [6, 7, 13–15] or for integration of structures possessing particular thermal properties with high-performance electronic or optoelectronic devices. In addition, recent studies of $Si/Si_{1-x}Ge_x$ superlattices have suggested that layer design can dramatically alter thermal transport characteristics [5, 16], and there has been work suggesting that quantum-well and quantum-dot structures can produce large reductions in thermal conductivity that impact thermal transport and thermal management in semiconductor heterostructure devices [17–19].

In such structures, characterization of thermal conductivity in subsurface regions and of local variations in thermal conductivity presents a particular metrological challenge. For epitaxial semiconductor structures, scanning probe microscopy (SPM) is typically employed with the sample in an in-plane geometry that provides access only to the epitaxially grown surface [10, 11, 20, 21]. Here, we present studies in which nanoscale cross-sectional thermal measurements are demonstrated that enable direct measurement and comparison of thermal properties across multiple materials via the $3\omega$ technique combined with SPM [10–12, 21]. By cleaving and, if needed, polishing to expose a smooth cross-sectional surface, properties of material beneath the final epitaxially grown surface can be characterized. In this measurement configuration, we can directly characterize thermal, electronic, and other material properties of interfaces and buried layers in heterostructures using scanned probe microscopy [22–24]. In this study, an ErAs/GaAs superlattice

 © 2015 IOP Publishing Ltd Printed in the UK

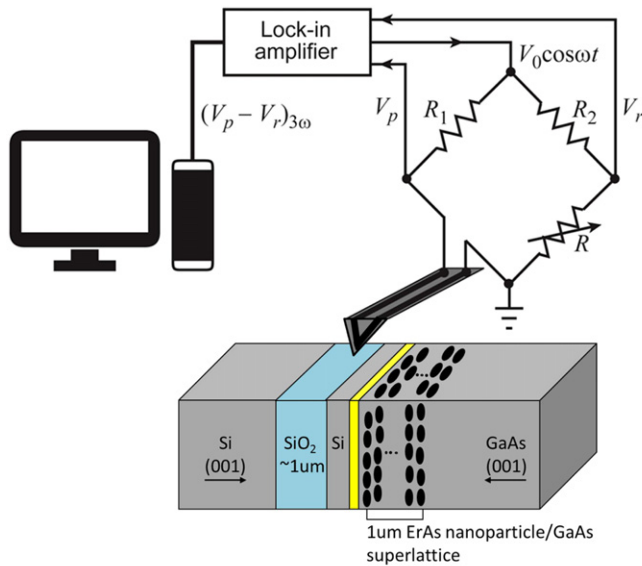


**Figure 1.** Schematic diagram of sample geometry, scanned thermal probe 3$\omega$ measurement apparatus, and associated electronic circuitry.

structure was employed in our analysis of thermal characteristics since the given structure is a highly promising candidate for thermoelectric devices application [25] because of the semimetallic properties of ErAs embedded in GaAs combined with decreasing thermal conductivity due to the phonon scattering from the ErAs/GaAs nanostructures [11, 15].

## 2. Experimental method

A schematic of the cross-sectional sample structure and scanning thermal measurement setup is shown in figure 1. The measurement apparatus and experimental geometry are analogous to those for the in-plane 3$\omega$ proximal probe method [11]. In brief, a functionalized thermal probe tip, VITA-DM-GLA-1 from Bruker, on which a thin patterned Pd film was fabricated on the $Si_3N_4$ substrate, was electrically excited at a frequency $\omega$. The electrical excitation induced Joule heating of the thermal probe at frequency 2$\omega$ and a corresponding resistance variation in the thermal probe with frequency 2$\omega$ [10, 12, 26, 27]. To detect temperature variations, the thermal probe was connected to one arm of a Wheatstone bridge circuit, as shown in the schematic of figure 1, with two other resistors, $R_1$ and $R_2$, of known value and one variable resistor used to balance the bridge. Temperature changes of the thermal probe caused its resistance to change and the differential signal $V_p$–$V_r$ at the 3rd harmonic frequency 3$\omega$, which contains temperature information, was detected by a Sr-830 lock-in amplifier and used to monitor the thermal interaction between probe tip and sample.

The ErAs/GaAs superlattice structure employed in this work was grown by solid-source molecular beam epitaxy (MBE) in a Varian Gen II system. The sample structure consisted of a 150 nm undoped GaAs buffer layer grown at 580 °C on a semi-insulating GaAs (001) substrate, followed by a ~1000 nm ErAs/GaAs superlattice consisting of 200 repetitions of 0.25 monolayer (ML) ErAs and 5 nm GaAs grown at 530 °C. Under these growth conditions, the ErAs layers form 3–4 ML (~0.9–1.1 nm) high nanoparticles [28, 29], leading to an average fill factor of ~6% for each ErAs layer. The exposed GaAs layer remaining after each ErAs deposition seeds the GaAs overgrowth, allowing high-quality overgrowth of the ErAs nanoparticles [30]. The surface of the ErAs/GaAs superlattice structure is covered by a 15 nm GaAs capping layer to prevent oxidation.

Initial SThM measurements were performed with a cross-section of the ErAs/GaAs superlattice structure after cleaving the sample and rotating it to access the cross-section of the sample area of interest as shown in supplementary figure 1. Initial dc scanning thermal microscope data showed that a thermal signal response was observed near the edge region where the ErAs/GaAs superlattice is located. However, the thermal signal observed in this configuration is actually an artifact originating from heat transfer to air at the edge of the sample structure, and is not due to the ErAs/GaAs superlattice sample itself, as shown in supplementary figure 2. (See supplementary information for detailed discussion.)

To eliminate this undesirable edge effect, additional samples were prepared using thermocompression bonding to bond ErAs/GaAs superlattice epitaxial layer structures front-to-front with another solid-state structure; a silicon on insulator (SOI) wafer was employed for this purpose so that multiple materials with different thermal conductivities could be imaged simultaneously. This approach enabled the epitaxial layers of interest to be embedded within a sample region away from any edges, and eliminated the spurious edge-induced signal variation in the sample region of interest. For the thermocompression bonding process, 30 nm Ti followed by 250 nm Au was deposited on both the superlattice and SOI wafer surfaces, with the Ti acting as an adhesion and diffusion-blocking layer [31]. The wafers, approximately 1.3 × 1.3 cm in area each, were then held together with a force of 2 kN at 320 °C for 15 min in a vacuum chamber. The bonded structure was then cleaved, and the exposed cross-sectional surface polished with 3 $\mu$m, 1 $\mu$m, and then 300 nm grit size polishing paper. This process routinely yielded polished surfaces with ~6 nm rms surface roughness. It is important to have a very flat sample surface after the polishing process, since the thermal signal can be susceptible to crosstalk from topographic features.

## 3. Experimental results and discussion

Figure 2(a) shows a schematic diagram of the bonded cross-sectional sample structure, along with topographic and 3$\omega$ voltage signal ($V_{3\omega}$) images obtained at an excitation frequency $f = \omega/2\pi$ of 1.2 kHz and ac voltage amplitude of 0.75 V. Measured total electrical resistance of thermal probe was 364 $\Omega$. NiCr limiter resistance is 200.34 $\Omega$ and Pd thermal probe tip resistance is 163.66 $\Omega$, respectively. During the data collection, to maintain a same loading force, deflection

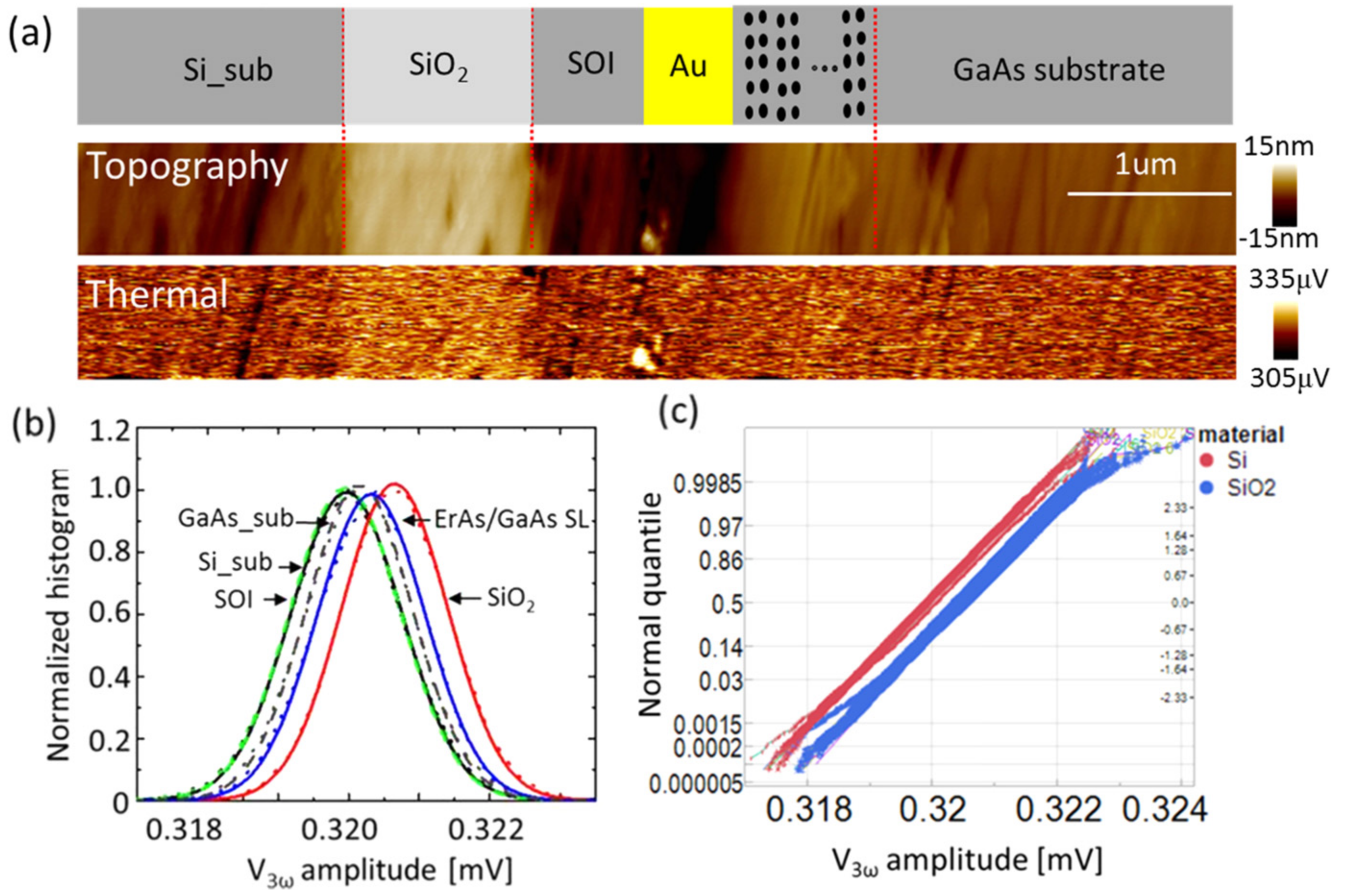


**Figure 2.** Cross-sectional scanning thermal microscopy of bonded SOI and ErAs/GaAs superlattice structure. (a) Schematic diagram of sample and measurement geometry, and topographic and thermal images of cross-sectional surface. (b) Normalized histograms (dots) for each designated region and fits to Gaussian distributions for each (lines and dashes). (c) Normal quantile plots for multiple measurements performed on $1000 \times 1000$ nm cross-sectional areas of the Si substrate (red) and $SiO_2$ layers (blue).

set point was set to 0.3. The cross-sectional area in the image encompasses, from left to right in the images, the Si substrate region of the SOI wafer, the buried oxide layer, thin Si layer, Au bonding layers, ErAs/GaAs superlattice, and GaAs buffer layer and substrate. Figure 2(b) shows normalized histograms of $V_{3\omega}$ signal amplitudes and Gaussian fits to these distributions for each designated region. From each material region, we take the peak position of the Gaussian distribution to be the signal level corresponding to that material. To assess the experimental uncertainty in determining this signal level for each material, we obtained multiple measurements for each material and compared the signal level distributions for each. Figure 2(c) shows a normal quantile plot of multiple measurement results for Si and $SiO_2$ sample regions [32, 33]. From the quantile plot, we can check that each material's thermal responses are normally distributed and they have clearly different distributions even though the width of each Gaussian distribution in figure 2(b) is quite large compared to their mean difference. T-tests for each material in figure 2(b) also confirm that their distributions are distinct.

Since each data point in thermal images such as those shown in figure 2(a) is influenced by a variety of factors including measurement duration, local surface roughness, and measurement noise, averaging a large number of points in an image for each material to obtain the average signal level, corresponding to the peaks of the Gaussian distributions shown in figure 2(b) and the 50th percentile values in figure 2(c), yields a characteristic signal level for that material. We then take the variation in this characteristic signal level across multiple measurements obtained in this manner to be the experimental uncertainty in determining this characteristic signal level for a given material.

Detailed modeling of thermal transport in the probe tip and sample structure, combined with model parameter calibration using $V_{3\omega}$ signals measured for materials of known thermal conductivity, enables quantitative, local determination of thermal conductivity in an unknown material [10–12]. We assumed a point contact of the thermal probe on the flat surface [11, 34]. Figure 3 shows the $V_{3\omega}$ amplitude calculated using such a model, following the approach of [11], along with the signal amplitudes for GaAs, $SiO_2$, Si substrate, thin Si layer, and ErAs/GaAs superlattice extracted from multiple measurements for each material in the manner described above. Au layer data fitting was intentionally excluded in the plot, since the thermal conductivity response is limited for high thermal conductivity materials [11, 35] as shown in figure 3. For GaAs, $SiO_2$, and the two Si layers, these values are plotted as a function of their known thermal conductivity.

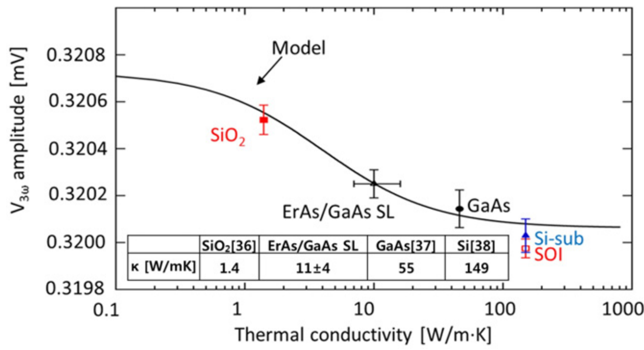


**Figure 3.** $V_{3\omega}$ amplitude predicted by numerical modeling and calibration to known thermal conductivities for Si, $SiO_2$, and GaAs (solid line), and measured mean values of $V_{3\omega}$ for $SiO_2$, ErAs/GaAs superlattice, GaAs, Si substrate, and thin Si layer. Horizontal positions of the measured signals were determined by using known thermal conductivities for GaAs, Si, and $SiO_2$, and by fitting to the numerical model for the ErAs/GaAs superlattice and corresponding thermal conductivity values are given in inset table.

As shown in figures 2(b) and (c), each material distribution is distinct and the mean value for each represents that material's thermal properties; multiple measurements for each material provided confidence intervals for each material's signal level. The vertical error bars in figure 3 correspond to the statistical distribution of mean values from multiple measurements for each material as described above. For $SiO_2$, GaAs, and Si, the material thermal conductivities were assumed to correspond to their established values which are given in the table in figure 3. The solid curve in figure 3 corresponds to the model for $V_{3\omega}$ signal response as a function of sample thermal conductivity, calibrated using the known thermal conductivities and measured signal values for GaAs, $SiO_2$, and Si. The thermal conductivity of the ErAs/GaAs superlattice is then taken to be that predicted by the calibrated model for the signal level measured experimentally for the superlattice. The resulting thermal conductivity of ErAs/GaAs, $11 \pm 4\ \mathrm{W\ m^{-1}\ K^{-1}}$ with confidence interval of 95%, agrees well with that determined from separate measurements reported elsewhere [11] and provides confirmation of the ability to obtain quantitative, local measurements of thermal conductivity in a cross-sectional geometry.

## 4. Conclusion

In conclusion, we have demonstrated the use of scanning thermal microscopy in a cross-sectional sample geometry to perform quantitative analysis of thermal conductivity in ErAs/GaAs superlattices grown by MBE. In doing so, we have elucidated the effects of thermal transport behavior near large topographic features such as abrupt edges or deep trenches in producing scanning thermal microscopy measurement artifacts, and shown that these effects can be eliminated by fabricating sample structures in which the epitaxial layers of interest are positioned away from the sample edge by bonding to an additional wafer followed by cleaving and polishing of the exposed cross-sectional surface. Furthermore, these measurements demonstrate an approach that allows thermal conductivity to be characterized for buried layers in semiconductor heterostructures, opening up the possibility of performing such measurements for a broad range of heterostructures, nanostructures, and semiconductor devices. We have obtained a room-temperature thermal conductivity for the ErAs/GaAs superlattice structure studied here of $11 \pm 4\ \mathrm{W\ m^{-1}\ K^{-1}}$, which confirms that ErAs/GaAs superlattice structures are able to reduce the thermal conductivity of the host material, GaAs, due to phonon scattering from ErAs nanoparticles.

## Acknowledgments

Part of this work was supported by NSF (DMR-1311866), ONR (N00014-10-1-0763), and the Judson S Swearingen Regents Chair in Engineering at the University of Texas at Austin.

## References

[1] Li D, Wu Y, Kim P, Shi L, Yang P and Majumdar A 2003 Thermal conductivity of individual silicon nanowires *Appl. Phys. Lett.* **83** 2934–6
[2] Hochbaum A I, Chen R, Delgado R D, Liang W, Garnett E C, Najarian M, Majumdar A and Yang P 2008 Enhanced thermoelectric performance of rough silicon nanowires *Nature* **451** 163–7
[3] Boukai A I, Bunimovich Y, Tahir-Kheli J, Yu J-K, Goddard Iii W A and Heath J R 2008 Silicon nanowires as efficient thermoelectric materials *Nature* **451** 168–71
[4] Chiritescu C, Cahill D G, Nguyen N, Johnson D, Bodapati A, Keblinski P and Zschack P 2007 Ultralow thermal conductivity in disordered, layered $WSe_2$ crystals *Science* **315** 351–3
[5] Pernot G *et al* 2010 Precise control of thermal conductivity at the nanoscale through individual phonon-scattering barriers *Nat. Mater.* **9** 491–5
[6] Kim W, Zide J, Gossard A, Klenov D, Stemmer S, Shakouri A and Majumdar A 2006 Thermal conductivity reduction and thermoelectric figure of merit increase by embedding nanoparticles in crystalline semiconductors *Phys. Rev. Lett.* **96** 045901
[7] Mingo N, Hauser D, Kobayashi N P, Plissonnier M and Shakouri A 2009 'Nanoparticle-in-alloy' approach to efficient thermoelectrics: silicides in SiGe *Nano Lett.* **9** 711–5
[8] Cahill D G, Ford W K, Goodson K E, Mahan G D, Majumdar A, Maris H J, Merlin R and Phillpot S R 2003 Nanoscale thermal transport *J. Appl. Phys.* **93** 793–818
[9] Minnich A J, Dresselhaus M S, Ren Z F and Chen G 2009 Bulk nanostructured thermoelectric materials: current research and future prospects *Energy Environ. Sci.* **2** 466–79
[10] Puyoo E, Grauby S, Rampnoux J-M, Rouvière E and Dilhaire S 2011 Scanning thermal microscopy of individual silicon nanowires *J. Appl. Phys.* **109** 024302
[11] Park K W, Nair H P, Crook A M, Bank S R and Yu E T 2013 Quantitative scanning thermal microscopy of ErAs/GaAs superlattice structures grown by molecular beam epitaxy *Appl. Phys. Lett.* **102** 061912
[12] Lefèvre S and Volz S 2005 $3_\omega$-scanning thermal microscope *Rev. Sci. Instrum.* **76** 033701

[13] Zide J M, Klenov D O, Stemmer S, Gossard A C, Zeng G, Bowers J E, Vashaee D and Shakouri A 2005 Thermoelectric power factor in semiconductors with buried epitaxial semimetallic nanoparticles *Appl. Phys. Lett.* **87** 112102
[14] Zeng G *et al* 2006 ErAs:InGaAs/InGaAlAs superlattice thin-film power generator array *Appl. Phys. Lett.* **88** 113502
[15] Kim W, Singer S L, Majumdar A, Vashaee D, Bian Z, Shakouri A, Zeng G, Bowers J E, Zide J M O and Gossard A C 2006 Cross-plane lattice and electronic thermal conductivities of ErAs: InGaAs/InGaAlAs superlattices *Appl. Phys. Lett.* **88** 242107
[16] Luckyanova M N *et al* 2012 Coherent phonon heat conduction in superlattices *Science* **338** 936–9
[17] Khitun A, Liu J and Wang K L 2004 On the modeling of lattice thermal conductivity in semiconductor quantum dot superlattices *Appl. Phys. Lett.* **84** 1762–4
[18] Tan H, Kamath K K, Mi Z, Bhattacharya P and Klotzkin D 2006 Analysis of the reduced thermal conductivity in InGaAs/GaAs quantum dot lasers from chirp characteristics *Appl. Phys. Lett.* **89** 121116
[19] Ge Z, Moat P, Xie J, Hu J, Huang J-S, Sun X, Li N, White B E and Klotzkin D 2012 Thermal conductivity of 1.3 $\mu$m InAs/GaAs quantum dot laser active material from chirp and 3$\omega$ measurements *Appl. Phys. Lett.* **100** 082108
[20] Shi L, Plyasunov S, Bachtold A, McEuen P L and Majumdar A 2000 Scanning thermal microscopy of carbon nanotubes using batch-fabricated probes *Appl. Phys. Lett.* **77** 4295–7
[21] Pumarol M E, Rosamond M C, Tovee P, Petty M C, Zeze D A, Falko V and Kolosov O V 2012 Direct nanoscale imaging of ballistic and diffusive thermal transport in graphene nanostructures *Nano Lett.* **12** 2906–11
[22] Rosenthal P A, Yu E T, Pierson R L and Zampardi P J 2000 Characterization of $Al_xGa_{1-x}As$/GaAs heterojunction bipolar transistor structures using cross-sectional scanning force microscopy *J. Appl. Phys.* **87** 1937–42
[23] Zuo S L, Hong Y G, Yu E T and Klem J F 2002 Cross-sectional scanning tunneling microscopy of GaAsSb/GaAs quantum well structures *J. Appl. Phys.* **92** 3761–70
[24] Rosenthal P A, Taur Y and Yu E T 2002 Direct measurement and characterization of n+ superhalo implants in a 120 nm gate-length Si metal–oxide–semiconductor field-effect transistor using cross-sectional scanning capacitance microscopy *Appl. Phys. Lett.* **81** 3993–5
[25] Zeng G *et al* 2006 ErAs:InGaAs/InGaAlAs superlattice thin-film power generator array *Appl. Phys. Lett.* **88** 133502
[26] Birge N O and Nagel S R 1987 Wide-frequency specific heat spectrometer *Rev. Sci. Instrum.* **58** 1464–70
[27] Cahill D G 1990 Thermal conductivity measurement from 30 to 750 K: the 3$\omega$ method *Rev. Sci. Instrum.* **61** 802–8
[28] Kadow C, Johnson J A, Kolstad K, Ibbetson J P and Gossard A C 2000 Growth and microstructure of self-assembled ErAs islands in GaAs *J. Vac. Sci. Technol.* B **18** 2197–203
[29] Nair H P, Crook A M and Bank S R 2010 Enhanced conductivity of tunnel junctions employing semimetallic nanoparticles through variation in growth temperature and deposition *Appl. Phys. Lett.* **96** 222104
[30] Crook A M, Nair H P and Bank S R 2011 Surface segregation effects of erbium in GaAs growth and their implications for optical devices containing ErAs nanostructures *Appl. Phys. Lett.* **98** 121108
[31] Chang L-B, Shiue C-C and Jeng M-J 2009 High reflective p-GaN/Ni/Ag/Ti/Au Ohmic contacts for flip-chip light-emitting diode (FCLED) applications *Appl. Surf. Sci.* **255** 6155–8
[32] Wang M C and Bushman B J 1998 Using the normal quantile plot to explore meta-analytic data sets *Psychol. Methods* **3** 46–54
[33] Chambers J M, Cleveland W S, Kleiner B and Tukey P A 1983 *Graphical Methods for Data Analysis* (Boston, MA: Duxbury Press)
[34] Shi L and Majumdar A 2001 Thermal transport mechanisms at nanoscale point contacts *J. Heat Transfer* **124** 329–37
[35] Bodzenta J, Kazmierczak-Balata A, Lorenc M and Juszczyk J 2010 Analysis of possibilities of application of nanofabricated thermal probes to quantitative thermal measurements *Int. J. Thermophys.* **31** 150–62
[36] Zhu M, Chu P K, Shi X, Wong M, Liu W and Lin C 2004 Formation of silicon-on-diamond by direct bonding of plasma-synthesized diamond-like carbon to silicon *Appl. Phys. Lett.* **85** 2532–4
[37] Gang C 2005 *Nanoscale Energy Transport and Conversion* (Oxford: Oxford University Press)
[38] Incropera F P and DeWitt D P 1996 *Fundamentals of Heat and Mass Transfer* (New York: Wiley)